




Spatiotemporal trends and evapotranspiration estimation using an improvised SEBAL convergence method for the semi-arid region of Western Rajasthan, India

Dhruv Saxena ^{*}, Mahender Choudhary  and Gunwant Sharma 

Department of Civil Engineering, Malaviya National Institute of Technology, Jaipur 302017, India

*Corresponding author. E-mail: dhruvsaxena.dstar@gmail.com, 2018rce9168@mnit.ac.in

 DS, 0000-0002-3438-9240; MC, 0000-0002-5619-7004; GS, 0000-0002-6698-9953

ABSTRACT

The study demonstrates how to estimate evapotranspiration (ET) for the Western Rajasthan region of India utilizing remotely sensed images with the Surface Energy Balance Algorithm for Land (SEBAL). Landsat 8 and Moderate Resolution Imaging Spectroradiometer (MODIS) satellite inputs were used to compute seasonal and annual ET on the Google Earth Engine platform. The assessment utilizing the SEBAL algorithm, in combination with the Food and Agriculture Organization (FAO) Penman–Monteith (PM) and Hargreaves methods, demonstrates that SEBAL has adequate reliability for estimating ET for a spatially large extent in semi-arid regions when evaluated with the Hargreaves method. The values of R^2 , root-mean-square error (RMSE), and mean bias error (MBE) for FAO-PM were 0.63, 1.65 mm/day, and 1.28 mm/day, respectively. For the Hargreaves method, the values of R^2 , RMSE, and MBE were 0.96, 0.41 mm/day, and -0.31 mm/day, respectively. The study showed that the northern region witnessed the highest ET due to the availability of abundant surface water for irrigation. Overall, the results demonstrate the SEBAL model's effectiveness in estimating evapotranspiration. A downward trend in ET is observed in the region, mainly due to changing climatic conditions.

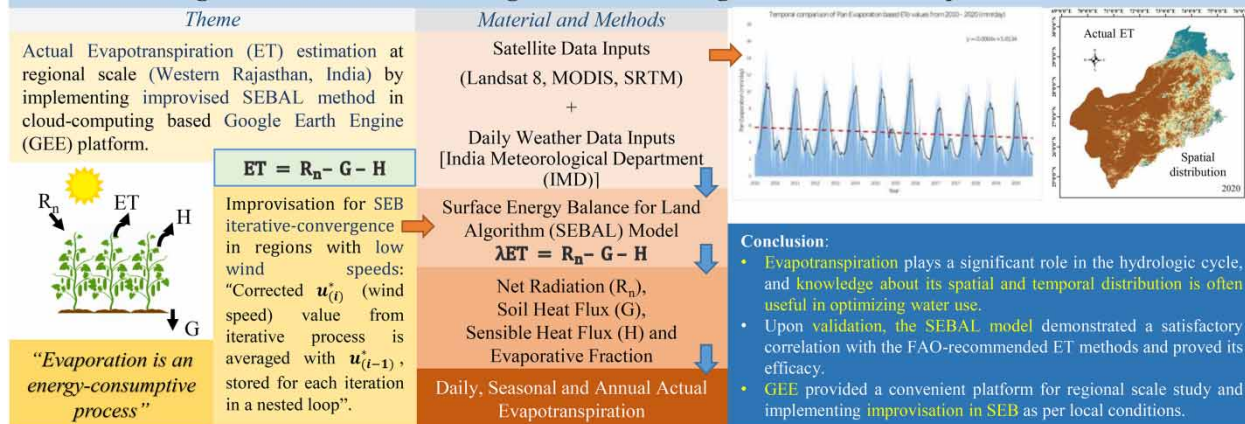
Key words: evapotranspiration, Google Earth Engine, remote sensing, SEBAL, semi-arid

HIGHLIGHTS

- Improvised SEBAL model integrated with GEE demonstrates satisfactory performance for regional scale ET estimation.
- Hargreaves method performed relatively better for selected semi-arid to arid study area.
- Study demonstrates an inverse correlation of LST with NDVI.
- Improvised SEBAL model leads to faster and more efficient convergence of the iterative process.
- Downward trend in pan evaporation-based ET observed.

GRAPHICAL ABSTRACT

Evapotranspiration estimation using improvised Surface Energy Balance convergence method integrated with remote sensing for semi-arid region of Western Rajasthan, India



1. INTRODUCTION

Calculating actual evapotranspiration (ET) is crucial as it regulates how much water and thermal energy is exchanged between the atmosphere and the ground surface. ET significantly affects the ecosystem of any region, and its assessment at a high spatial and temporal resolution plays a crucial role in the integrated management and planning of agricultural water supplies. Therefore, many mathematical models and algorithms have been planned to assess quantitative values of evapotranspiration. Calculation methods either use the inputs available from meteorological stations or other mediums such as gridded and reanalysis data where there is a lack of data from meteorological stations.

In canal-based irrigation commands, the irrigation schedule is either done based on the farmer’s demand or on the calendar days passed since the last irrigation. Compared to the rotational water distribution system, canal water supply based on actual crop water demand is of great importance. ‘The National Commission on Integrated Water Resources Development (NCIWRD-1999) had projected the efficiency of India’s surface irrigation systems as forty, fifty, and sixty per cent in the years 2010, 2025, and 2050, respectively’ (Amarasinghe *et al.* 2007). Ground-based flux measurement methods like the Bowen Ratio (BR) method (Bowen 1926), Eddy covariance (EC) method (Wilson *et al.* 2002), and the recent Surface Renewal (SR) alpha calibration method (Shapland *et al.* 2014) can furnish ET measurements with high temporal scales such as half-hourly to daily. However, these methods cannot capture diversification within the plantation fields due to their low spatial trace. Furthermore, these methods need expensive equipment for data collection, and their maintenance demands intensive labor.

The objective of the present study is to evaluate the feasibility of the application of the SEBAL model in the region to estimate the actual evapotranspiration. Optimization in irrigation scheduling would facilitate the decision-makers and will reduce losses, improve irrigation efficiency and maintain the crop yield. With recent advancements, the radiative energy interchange among the Sun, Earth, and space can be evaluated more precisely utilizing new satellite technologies. The plant’s growth stage or level of maturity, solar radiation, wind speed, temperature, relative humidity, and percentage of soil cover are some of the key factors that affect evapotranspiration. A standard measurement of ET at a spatially large variation is quite complex. Therefore, remote sensing and Geographic Information System (GIS) approaches were applied to evaluate ET from available satellite and meteorological data to estimate ET over such a large spatial extent accurately.

In the past five decades, numerous methods have been developed to calculate ET_o according to climatic conditions and available meteorological data. To improve the performance of the ET_o evaluation, the United Nation’s (UN) body – the Food and Agriculture Organization (FAO) – has propounded four methods, including the modified Penman method, radiation method, pan evaporation method, and Blaney–Criddle method. However, these methods often give varying ET_o results among different locations and have large deviations (Pereira *et al.* 2015). Among various methods, Priestly-Taylor and Hargreave’s methods show results with high accuracy in the arid and semi-arid regions (Gao *et al.* 2017). In recent decades, with increasingly available free satellite observations from multiple sensors, various methods have been implemented

across the world (Elkatoury *et al.* 2020). Shamloo *et al.* (2021) estimated ET and crop coefficient of corn in the Mediterranean region of Adana province in Turkey using the SEBAL algorithm. Aryalekshmi *et al.* (2021) reviewed various surface energy balance (SEB) models for ET estimation using remote sensing data. Wu *et al.* (2010) applied SEBAL and Markov models for simulating future streamflow. Empirical algorithms have been built and demonstrated that connect ET with vegetation indices obtained from satellite observations and meteorological data (Johnson & Trout 2012). Studies suggest, ‘These models perform well in areas where they are calibrated, but uncertainty increases when applied to other areas.’ However, the Hargreaves method, calibrated with weather measurements of arid and semi-arid regions, has shown optimistic results for assessing ET integrated with remote sensing (Shamloo *et al.* 2021).

Three substantially important forms of ET can be expressed as actual evapotranspiration (ET_a), potential evapotranspiration (ET_p), and reference evapotranspiration (ET_o). ‘ ET_p is the water loss which would occur when sufficient moisture is available in the soil such that stomata are fully open and resistance to water vapor transport from bare soil to the atmosphere is at a minimum’ (Beaumont Blake & Wagstaff 2016). ET_o is defined by a theoretical surface with no restrictions on the availability of soil moisture as the reference evapotranspiration rate (Allen *et al.* 1998). ET_a is the disappearance of water through a surface under vegetation with prevailing soil moisture conditions. ET_o can significantly vary on a daily timescale. However, several studies have reported ET_o spatially very consistent at the regional scale unless where there are significant topographical slopes (Zhang *et al.* 2019).

Stationary actual evapotranspiration (ET_a) estimation methods have multiple drawbacks when the spatial extents are very large (10 hectares or more). Major drawbacks include issues such as measurement of point data for a specific region, maintenance problems, estimation of the hydrological process that is of a complex nature, and the need for expert workers. To resolve these prominent issues, a method such as the ‘Surface Energy Balance Algorithm for Land’ (SEBAL) model, which is based on remotely sensed images, can be utilized. When compared to other SEB models, SEBAL has performed well for ET studies at regional scales for diverse climatic conditions and scarce meteorological data (Li *et al.* 2009; Wanniarachchi & Sarukkalgige 2022). Presently available remote sensing-based ET and reanalysis datasets with global gamut comprise the 1 km – Moderate Resolution Imaging Spectroradiometer (MODIS) data products (Rahimi *et al.* 2015) and reanalysis records such as MERRA-2 (Lv *et al.* 2021) having 8-day and 1-month temporal resolutions, respectively, which are considered coarse for various regional-level hydrological applications. Using the FAO Penman–Monteith (FAO-PM) and Hargreaves Method as a benchmark, we evaluated the accuracy of daily ET generated from remote sensing data vs. ET derived from observation/station data using the FAO-PM and Hargreaves Method. We compared which method performs best in arid and semi-arid regions and investigated the dominant drivers of ET spatial and temporal variation in Western Rajasthan. Therefore, a semi-automated code using Google Earth Engine (GEE) was developed, enabling the assessment of ET for the study region (arid and semi-arid). Following the development of the algorithm, a thorough assessment of the large Western Rajasthan region’s major crops and spatiotemporal cropping patterns with growth stages was identified using various studies (Jangid *et al.* 2018) and data available from the Department of Economics & Statistics under the Department of Planning (Agricultural Statistics 2020) and the Department of Agriculture, Government of Rajasthan (Crop Wise Sowing Area Report 2020).

The primary objectives of the present research are (a) to generate a spatiotemporal distribution of evapotranspiration of the western region of Rajasthan, India, and (b) to develop a remote sensing-based semi-automated evapotranspiration modeling framework.

2. STUDY AREA

The Indira Gandhi Nahar Pariyojana (IGNP) is one of the few such projects in the world with the objective of remodeling the desert wasteland into a productive area in terms of its agronomy. IGNP covers the western parts of the Rajasthan state, encompassing a large portion of the ‘Thar Desert’. As per the ‘Indus Water Treaty, India got the exclusive rights to use the waters of three rivers – Ravi, Beas, and Sutlej. Rajasthan got a share of 10.6 BCM from the surplus to develop the desert areas’. Major objectives have been building drought resilience, providing good quality drinking water, improving the environment along with developing and safeguarding animal wealth, and increasing agricultural production. IGNP comprises an extensive canal network with a long main canal emerging from Harike Barrage in the state of Punjab and a 3,400-km-long distribution system. The main canal extends up to Mohangarh (Jaisalmer district), which was completed in 1986. Farmers rely mainly on canal irrigation and groundwater (moderate to highly saline) for irrigation. The location map shows the command area of the project (Figure 1).

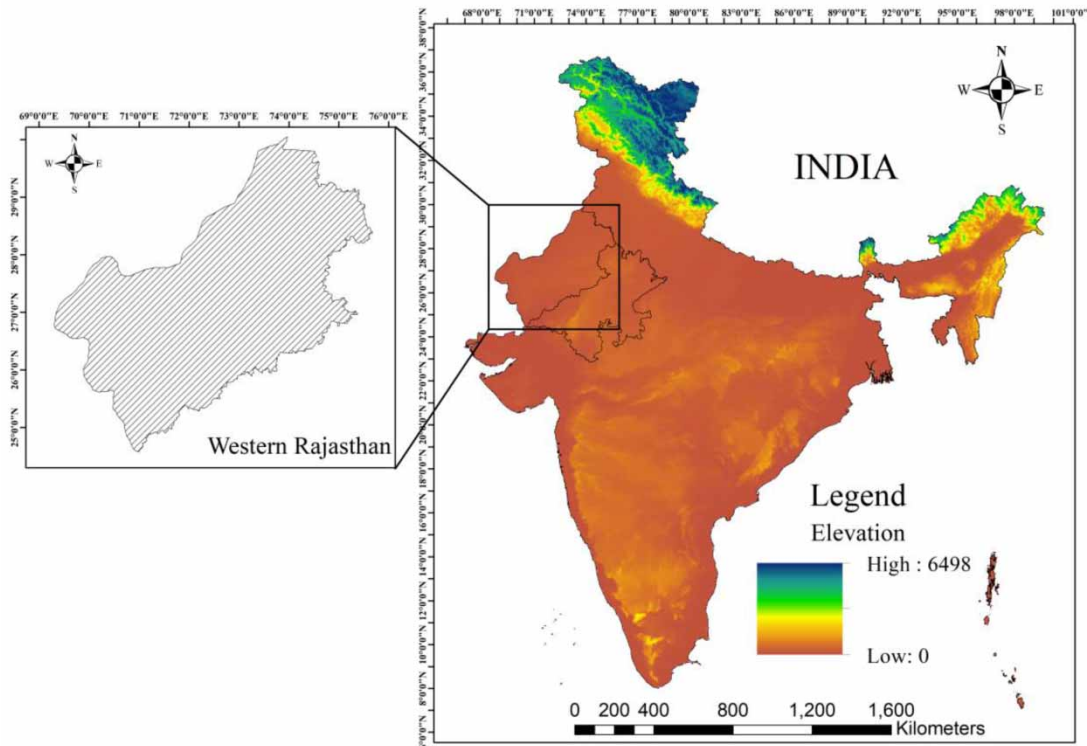


Figure 1 | Study area map – IGNP command area (left); elevation (in m).

The study area encompasses regions of IGNP in Sri Ganganagar, Hanumangarh, and Churu in the north-western parts of Rajasthan, Bikaner, Jaisalmer, and Barmer in the west, and Jodhpur and Nagaur in the central-west districts of Rajasthan, stretching a terrestrial extent of 1,72,050 km². The mean elevation is 211 m above sea level. The climatic characteristics of arid regions are low and erratic precipitation compared to high atmospheric demands. This region gets annual rainfall in the range of 100 to 500 mm with high rates of atmospheric water demand, i.e., evapotranspiration (Moharana *et al.* 2016). The IGNP command area map with Stage I and Stage II canal flow areas was acquired from the Department of Water Resources (WRD), Govt. of Rajasthan (Physical Progress 2020). Moharana *et al.* have comprehensively discussed the major landforms and desertification status of Western Rajasthan (Moharana *et al.* 2016).

3. MATERIALS AND METHODS

3.1. Remotely sensed data

Three sources of remotely sensed datasets were used in this study for the years 2019 and 2020. The United States Geological Survey (USGS) provided Landsat 8 surface reflectance observations that had been atmospherically rectified utilizing the ‘Land Surface Reflectance Code (LaSRC) algorithm’. The ‘Shuttle Radar Topography Mission (SRTM) digital elevation (Data Version 4)’ dataset was used to assess the topography of the region. The MODIS Terra Land Surface Temperature (LST) and emissivity inputs with a spatiotemporal resolution of 8-day Global 1 km from the USGS were used to obtain LST values. Landsat 8 with two thermal bands—10 and 11—is sufficient for obtaining LST and emissivity values (Jiménez-Muñoz *et al.* 2014), but to avoid temporal gaps in final results, MODIS Terra LST product was used in this study. Many studies have demonstrated the satisfactory application of Landsat-MODIS-based fusion models for ET estimation integrated with SEB methods (Bhattarai *et al.* 2015). The remote sensing data were accessed within the GEE framework.

3.2. *In situ* measurements

The local weather parameters required for the SEBAL model were acquired from the Indian Meteorological Department (IMD) station installed in Jodhpur City at 26.2578° N and 72.9952° E. The meteorological data obtained have a daily temporal

resolution and include various parameters, as shown in Table 1. Daily values of ET_o are measured utilizing the meteorological data using the FAO-PM and Hargreaves equations integrated with crop coefficient values (K_c).

4. METHODOLOGY

In the present study, the SEBAL algorithm-based model was applied for the assessment of ET over the study region. SEBAL utilizes digital images produced by sensors such as Landsat that can capture radiation throughout the visible, near-infrared, and thermal infrared bands. Developed by Bastiaanssen *et al.* (1998), the SEBAL model has become a valuable tool in various fields, such as agriculture, hydrology, and environmental studies. It operates on the basic principle of energy balance at the land surface. The general equation of SEBAL Equation (1) considers various components of the energy balance equation, including incoming solar radiation, outgoing radiation, sensible heat flux, soil heat flux, and latent heat flux. The SEBAL model relies on accurate meteorological input data and the availability of high-quality satellite imagery. Additional data requirements include LST and surface albedo. For this study, the median composite was generated using the power of the gigantic computation resources within a cloud-computing environment by analyzing more than 40 petabytes of geospatial data provided within the GEE framework (Gorelick *et al.* 2017). A simple linear regression-based fusion model was utilized to integrate Landsat and MODIS data (Bhattarai *et al.* 2015). The combination of remote sensing and GEE capabilities helps in achieving new levels of remote sensing modeling studies. This semi-automated code is particularly proposed in this study to evaluate ET obtained on a regional scale using an improvised SEBAL iterative convergence method, which is particularly useful during the computation of the sensible heat flux (H) when the measured wind speeds are low. The results obtained were validated using location-specific meteorological data. Also, as the study region is mostly flat in topography, the terrain influence is minimal.

The daily ET was evaluated based on the SEBAL algorithm (Figure 2) for the years 2019 and 2020 by employing the inputs from Landsat 8 and MODIS data, and 2 years' mean results were considered to reduce the variability in the actual ET assessment. By applying the cloud cover filter, cloud-free images were obtained to generate the seasonal and annual ET. More specifically, the 30-m Landsat-8 surface reflectance inputs were employed to calculate vegetative indices and albedo using well-known methods (Silva *et al.* 2016). In conjunction, statistics from the Department of Agriculture, Government of Rajasthan, were used to identify the principal crops planted over different seasons (Crop Wise Sowing Area Report 2020). The principal crops with their crop cycle have been described in Supplementary material, Table S4. To determine mean K_c values for the different analysis periods, statistical analysis was performed for the region's crop cycles to generate weighted averages, standard deviations, and variances, among others, for the years 2019 and 2020.

The procedure for computing ET is established on the energy balance, in which the quantity of ET is derived from the amount of energy remaining in the classical equation of energy balance, as shown in Equation (1). The amount of ET can be computed by deducting the net radiation from the heat fluxes into the air and soil (Bastiaanssen *et al.* 1998). The general equation of SEBAL used is

$$\lambda ET = R_n - G - H \quad (1)$$

Table 1 | Input data and source of data used for the study

Meteorological data input	Source
Temperature (daily)	India Meteorological Department (IMD)
Relative humidity (daily)	
Wind speed (daily)	
Sunshine hours (daily)	
Satellite data input	USGS
Landsat 8 (30 m, 16 days)	
MODIS Terra LST (1 km, 8 days)	
SRTM DEM Data version 4 (90 m)	

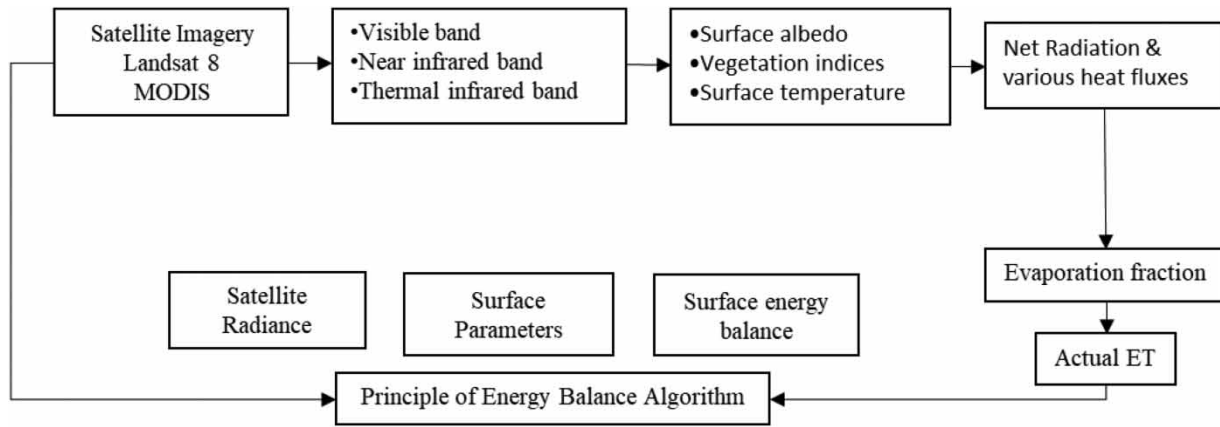


Figure 2 | Principle of SEBAL algorithm.

where the latent heat flux (W/m^2) is expressed as λET , the term R_n expresses the net radiation (W/m^2), and H determines the sensible heat flux (W/m^2). Methods for computing these elements are described below:

4.1. Net radiation flux (R_n)

Bastiaanssen *et al.* (1998) proposed to compute the net radiation as the difference of radiation fluxes at the ground (W/m^2) using the short-wave radiation coming toward the ground surface ($R_{s\downarrow}$). A fraction of this energy gets reflected due to different surfaces and is represented by $R_{s\uparrow}$, long-wave radiation incoming ($R_{L\downarrow}$), and long-wave radiation outgoing ($R_{L\uparrow}$). R_n is further computed using atmospheric transmissivity value, which is obtained from short- and long-wave radiation derived from the thermal bands for each pixel (Bastiaanssen *et al.* 1998) using Equation (2):

$$R_n = (1 - \alpha)R_{s\downarrow} + R_{L\downarrow} - R_{L\uparrow} - (1 - \epsilon_0)R_{L\downarrow} \tag{2}$$

where the term α is expressed as surface albedo, and ϵ_0 is expressed as the thermal surface emissivity (dimensionless).

4.2. Short-wave radiation reaching the ground surface ($R_{s\downarrow}$)

The short-wave radiation reaching the ground surface ($R_{s\downarrow}$) is calculated as follows:

$$R_{s\downarrow} = G_{sc} \times \cos \theta \times d_r \times \tau_{sw} \tag{3}$$

where G_{sc} is expressed as the solar constant ($1,367 W/m^2$). $\cos \theta$ is the cosine of the angles of incidence of solar radiation, and the value of θ is derived from the image data header file. d_r is represented as the ‘inverse of the square of the Earth’s relative distance to the Sun’ (Allen *et al.* 2005b).

4.3. Outgoing/reflected long-wave radiation ($R_{L\uparrow}$)

By utilizing Stefan–Boltzmann’s relation, the outgoing long-wave radiation flux is computed as

$$R_{L\uparrow} = \epsilon_0 \times \sigma \times T_s^4 \tag{4}$$

where ϵ_0 is the ‘broadband surface emissivity’, σ is the ‘Stefan–Boltzmann constant ($5.67 \times 10^{-8} W/m^2/K^4$)’, and T_s is the ‘surface temperature’ expressed in Kelvins.

4.4. Incoming long-wave radiation ($R_{L\downarrow}$)

The Stefan–Boltzmann formula is applied to compute the value of $R_{L\downarrow}$, which is computed as

$$R_{L\downarrow} = \epsilon_0 \times \sigma \times T_a^4 \tag{5}$$

where T_a is the temperature of the air near the surface and is replaced by the temperature observed at the cold pixel ($T_{\text{cold_pixel}}$). Below is a description of the procedure for selecting anchor pixels (hot and cold).

4.5. Soil heat flux (G)

An empirical fraction of the net radiation flux (R_n) using the computed Normalized Difference Vegetation Index (NDVI), surface temperature (T_s), and surface albedo (α) using the methodology proposed by Bastiaanssen (2000) is applied to obtain the value of G :

$$\frac{G}{R_n} = \frac{T_s}{\alpha(0.0038\alpha + 0.0074\alpha^2)(1 - (0.98)\text{NDVI}^4)} \quad (6)$$

4.6. Sensible heat flux (H)

The sensible heat flux is calculated by Equation (7) and determined by the thermal exchange to the air via molecular convection (Bastiaanssen 2000).

$$H = \frac{(\rho \times c_p \times dT)}{r_{ah}} \quad (7)$$

where ρ is the density of air (kg/m^3), C_p is the air heat (specific) having a value of $1,004 \text{ J kg}^{-1} \text{ K}^{-1}$, dT is the difference of temperature values at the height of z_1 and z_2 , which is computed as $T_1 - T_2$ (K), and r_{ah} represents the aerodynamic resistance to the heat exchange (s/m). All the parameters of this correlation depend on the surface roughness, temperature gradient, and prevailing wind speed. The two unknowns, consisting of r_{ah} and dT , make it very challenging to evaluate. Therefore, an iterative method proposed by Allen *et al.* (2005a) is used to compute these two unknowns. The iterative procedure begins by assuming neutral stability for estimating sensible heat flow by applying atmospheric stability corrections, which are based on the Monin–Obukhov model (Null 1996).

The near-surface temperature difference is expressed by the parameter dT (K). Due to uncertainty in radiometric/atmospheric calibration or contamination of the sensor, it is difficult to estimate surface temperature accurately from a satellite. Additionally, T_s is the surface temperature as measured by the MODIS satellite.

$$dT = a + bT_{s \text{ datum}} \quad (8)$$

As pioneered by Bastiaanssen, dT in Equation (8) can be approximately estimated as a relatively simple linear function of T_s (Bastiaanssen 2000). Using a digital elevation model (DEM), each pixel $T_{s \text{ datum}}$ (surface temperature) is assigned to a common elevation data, and a and b are further determined. The two coefficients need the sampling of two anchor pixels, designated as the hot and cold pixels, which reflect the near-extreme circumstances of temperature and relative humidity. The cold pixel is identified as a fully covered, well-irrigated crop surface. λET is supposed to be zero for the dry, barren farming represented by the hot pixel. These two anchor pixels are used to calculate all other pixels between them.

The SEBAL model is improvised as the measured meteorological data show relatively low wind speeds across the year, which results in difficulty in quantifying the value of aerodynamic resistance (r_{ah}) and the various components that are computed indirectly. Errors in r_{ah} affect the concluding value of H and dT , which are calculated using Equation (7). Using the modified iterative procedure of the SEBAL as proposed by Dhungel *et al.* (2016), the convergence of Monin–Obukhov stability correction was expedited. The method of improvisation in the convergence mechanism for the iterative process suggested by Dhungel *et al.* states that ‘The first iteration generates the set of data for the next iterations by averaging the u^* from the current time-step [$u_{(i)}^*$] and the previous time-step [$u_{(i-1)}^*$], which is stored for each iteration in a nested loop’ (Dhungel *et al.* 2016). The pixel was unable to achieve convergence from the previous method and either needed a large number of iterations or resulted in divergence in various instances.

The non-convergence would either result in over-estimating or under-estimating r_{ah} , which influences the final values of dT , H , and latent heat flux. After the averaging modification, convergence was achieved in a few iterations (less than 10), and the oscillation behavior was eliminated in this study. It has been demonstrated by Dhungel *et al.* (2016) that for higher wind speeds, the convergence behavior was similar before and after the modifications. This modification decreased the uncertainty

in flux calculations caused by non-convergence, enhancing the precision of SEB parameters, which is particularly relevant in arid and semi-arid climates (Dhungel *et al.* 2016). The results of this study confirm that averaging the components present in the nested loop helped expedite the process and achieve convergence in low wind speed conditions.

4.7. Daily evapotranspiration

Initially, λET , represented as the instantaneous latent heat flux, is computed, which represents the instantaneous heat from the ground surface generated because of ET at the instant of the satellite’s overpass. Finally, the instantaneous evaporative fraction is computed using Equation (9):

$$\Lambda = \frac{\lambda ET}{\lambda ET + H} = \frac{\lambda ET}{R_n - G} \tag{9}$$

where Λ is the instantaneous evaporative component, which is defined as ‘the ratio of actual to crop evaporative demand when atmospheric moisture conditions and soil moisture conditions are in equilibrium.’ It has been demonstrated by various studies that during the daytime, Λ is nearly constant, allowing for its usage as a temporal integration factor (Crago 1996; Jiang *et al.* 2021; Liu 2021). For timeframes equal to or greater than 1 day, the value of G can be disregarded, and the net energy available ($R_n - G$) gets reduced to net radiation (R_n). For daily timeframes, ET_{24} can be calculated as in Equation (10).

$$ET_{24} = \frac{86400 \times 10^5}{\lambda \rho_w} \Lambda R_{n24} \tag{10}$$

where R_{n24} ($W m^{-2}$) is represented as the 24-h mean net global radiation calculated using da Silva *et al.* (2015), λ ($J kg^{-1}$) is represented as the latent heat of vaporization, and ρ_w ($kg m^{-3}$) is expressed as the density of water. All computation for this research has been performed within the GEE environment and sheets (Excel) to calculate reference evapotranspiration (ET_o).

4.8. Seasonal evapotranspiration

The spatial distribution of ET across a full season is depicted on a seasonal ET map, which is often useful and can be deduced from the daily evapotranspiration data by extrapolating the ET_{24} values proportionally to the ET_o . It is assumed that the ET for the entire region varies in proportion to the changes in ET_o at the weather station.

$$ET_{period} = ET_r F_{period} \sum_1^n ET_{r-24} \tag{11}$$

where $ET_r F_{period}$ is the reference ET fraction representing the timeframe, ET_{r-24} is expressed as the daily ET (ET_{24}), number of days in the season is represented by n . Units of ET_{period} shall be measured in mm, while ET_{r-24} is in mm/day. The value of $ET_r F_{period}$ for different seasons is calculated by dividing the ET_{24} by the cumulative reference ET (ET_o) for that particular day.

4.9. Reference evapotranspiration (ET_o) estimation

Two methods were used in this study to estimate ET_o , FAO-PM (Equation (12) and Hargreaves method (Droogers & Allen no date) (Equation (13)), and was also correlated with the pan evaporation data obtained from the weather station. To estimate ET_o as per standard conditions for the median image, crop coefficients were identified, as shown in Table 2.

Table 2 | Crop coefficient in each of the seasons and phases of major crop growth cycle in the study area

Crop coefficient	Season	Crop growth stage
0.6	Pre-monsoon	Winter crops harvested, Zaid crops (early stage) in some regions
1.05	Monsoon	Summer crops (growth)
1.15	Post-monsoon	Summer crops (mid-growth)
1.2	Winter	Winter crops (mid-growth)

The two methods applied in this study require meteorological parameters, as described in Table 1. The equations for PM and Hargreaves methods are as follows:

$$ET_o = \frac{0.408\Delta(R_n - G) + \gamma \frac{900}{T_a + 273} U_2(e_s - e_a)}{\Delta + \gamma(1 + 0.34U_2)} \quad (12)$$

$$ET_o = 0.0023 (T_{mean} + 17.8) \times (\sqrt{T_{max} - T_{min}}) R_a \quad (13)$$

where ET_o is represented for ref-ET rate (mm day^{-1}), U_2 is the daily mean wind speed measured at 2 m height (m s^{-1}), Δ is the slope of the chart of vapor pressure versus temperature ($\text{kPa } ^\circ\text{C}^{-1}$), R_n is the net radiation density ($\text{MJ m}^{-2}\text{day}^{-1}$), G is the soil heat flux density ($\text{MJ m}^{-2}\text{day}^{-1}$) – considered to be zero because it is negligible at the daily timescale (Allen *et al.* 1998), T_a represents the mean daily air temperature ($^\circ\text{C}$), e_s represents the saturation vapor pressure (kPa), e_a is the actual vapor pressure (kPa), $e_s - e_a$ represents the vapor pressure deficit at saturation level (kPa), γ represents the psychrometric constant ($\text{kPa } ^\circ\text{C}^{-1}$), T_{mean} is the mean temperature ($^\circ\text{C}$), and R_a represents the extra-terrestrial radiation ($\text{MJ m}^{-2}\text{day}^{-1}$).

The evapotranspiration was evaluated by the SEBAL algorithm for the IGNP region. Furthermore, to validate the ET results obtained from the SEBAL model, various statistical parameters such as determination coefficient, root-mean-square, and mean bias error (MBE) of the values computed from SEBAL with the values obtained from the ET_o calculation using the Excel sheet were evaluated, as shown in Figure 7.

5. RESULTS AND DISCUSSIONS

The SEBAL model was used to calculate daily and seasonal actual evapotranspiration for the years 2019 and 2020 using Landsat 8 and MODIS Terra images integrated with meteorological data collected from a weather station. To validate the actual evapotranspiration calculated by SEBAL, FAO-PM and Hargreaves methods were used. Major crop coefficients for various seasons were estimated using statistical methods from the studies and data obtained from Rao & Poonia (2011), Shahrokhnia & Sepaskhah (2013), and Crop Wise Sowing Area Report (2020).

The seasonal variations in LST and NDVI (Supplementary Material, Figure S10) for 2 years are demonstrated. During the pre-monsoon period (April to mid-June), LST is high in Western Rajasthan, ranging from 23 to 45 $^\circ\text{C}$. Low temperatures correspond to agricultural lands in the northern part. Moderate to high LST is recorded over the arid western sections of the region, which is a major part of the Thar Desert. The monsoon season (July to mid-September) shows a reduction in LST mainly due to rainfall and cloudy weather. It also becomes difficult to obtain cloud-free images during this season, but with the abilities of GEE, it is possible to develop a representative median image without much complexity. This is also the period of highest precipitation. However, the observed LST is lower than in the pre-monsoon season. The LST during the post-monsoon season (October–November) ranges from 12 to 37 $^\circ\text{C}$. In this season, the Kharif crops (the local name for summer crops) are harvested, and the LST observed over the fallow agricultural lands is higher when compared to vegetated areas. The winter season (December–February) is the crop-growing Rabi (local name for winter crops) season. The winter LST ranges from 5 to 26 $^\circ\text{C}$, with low LST in the study area's northern and middle regions and comparatively high LST in the non-vegetated barren areas.

The NDVI index of the pre-monsoon period ranges between -0.2 and 0.45 in different time periods. Most of the region consists of barren land and fallow agricultural areas, as this is the season when the winter crops have already been harvested, showing low NDVI. Zaid crops (local name for crops between winter crops and summer crops) are grown in some of the northern and eastern regions of the study, which demonstrates relatively higher NDVI. The locations that have a low NDVI also correspond to the locations that have a high LST.

A representative pixel of the ET of the agricultural fields in proximity to the weather station was chosen to assess the execution results. The parameters obtained in the northern regions were examined afterward, and the final ET product was evaluated. Table 3 displays the statistics of the representative pixel for the years 2019 and 2020.

The representative pixel was chosen on the basis of regional knowledge of agricultural patterns followed in various seasons. It was based on the density of vegetative coverage of the major crops of the season. The presence of moisture in vegetation results in higher sensible heat flux for timescales, corresponding to higher NDVI. The values of G are proportional to the values of R_n , and when R_n is high, soil heat flux (G) is also high.

Table 3 | Statistics of the important components acquired from the SEBAL model for the selected/representative pixel for years 2019 and 2020

Median image (season-wise)	NDVI	Albedo	LST (°C)	Rn (W/m ²)	H (W/m ²)	G (W/m ²)	ET _{SEBAL} (mm/day)	ET _{o-PM} (mm/day)	ET _{o-HG} (mm/day)
Pre-monsoon (2019)	0.16	0.34	45.95	668.47	163.53	168.12	4.98	6.33	4.38
Monsoon (2019)	0.61	0.30	28.53	656.62	-16.3	84.98	6.20	7.90	5.58
Post-monsoon (2019)	0.73	0.26	35.61	693.59	42.97	90.66	4.97	7.82	4.67
Winter (2019)	0.71	0.22	23.72	638.92	178.38	55.8	3.73	3.95	3.74
Pre-monsoon (2020)	0.17	0.32	45.71	652.17	235.24	160.86	4.56	7.30	4.54
Monsoon (2020)	0.63	0.29	29.29	646.89	-20.2	95.91	6.28	7.41	5.51
Post-monsoon (2020)	0.62	0.28	38.72	674.76	62.59	97.42	4.75	4.70	4.45
Winter (2020)	0.78	0.23	22.64	629.47	154.21	44.53	3.82	3.98	3.81

The NDVI for the monsoon ranges between -0.15 and 0.84. The maximum NDVI values are recorded in the northern sections of farmlands, while the lowest NDVI values are observed over arid and agricultural fallow. Following the monsoon season, the NDVI ranges from -0.18 to 0.89 in the post-monsoon season. The development of vegetation caused by the monsoon season resulted in a higher NDVI during the post-monsoon period. The wintertime NDVI ranges from -0.42 to 0.83. Over the northern and central portions of the study area, which consist of agricultural fields, a high NDVI is found.

The NDVI demonstrates greater values when the observed LST is low. Many studies have also demonstrated such an inverse linear relationship between NDVI and LST (Kalluri *et al.* 1998; Kumar & Shekhar 2015; Tran *et al.* 2017; Kundu *et al.* 2018). NDVI is higher in vegetated lands, and after crop harvest, NDVI decreases. The direct surface heating is restrained as the higher leaf area index (LAI) captures the incident solar radiation. Furthermore, it alters the energy flux at the surface because of the constant cooling and evapotranspiration from the surface (Babatunde 2012).

5.1. Seasonal and annual ET of 2019 and 2020

The spatial distribution of annual and seasonal (timescales) actual ET of various seasons is given in Figures 3 and 4.

In the pre-monsoon season, the northern and mid-eastern parts show high ET, which consists of agricultural areas. The western region is mostly barren and, hence, shows negligible ET. As the winter crops are harvested in this season, low ET is observed when correlated to the monsoon season. The monsoon season shows elevated ET values in the agricultural fields (northern and mid-eastern regions) for various reasons, such as higher availability of surface water (from rainfall) combined with high air temperatures. Also, Kharif crops (summer crops) are grown during this season, exhibiting high transpiration rates. However, the surface temperature values observed are lower than in the pre-monsoon season because of the cooling effects of overcast skies and rainfall during this season.

Low ET is detected over the farmlands in the northern and mid-eastern regions in the post-monsoon season, which are mainly fallow lands as the summer crops are harvested during the months of October to November. High evapotranspiration is observed in agricultural areas in the winter period as this is the Rabi crop's (winter crop) growth phase. Rabi crops are mainly grown in canal-irrigated areas and regions with available access to groundwater of desired quality. Across all seasons, it is observed that NDVI varies with ET, as demonstrated in Figures 3 and 4. The crop calendar for major crops is depicted in Supplementary material, Table S1.

The annual ET ranges from negligible in barren western regions and 57.82 to 2,346.24 mm in other areas, as per the FAO-PM method. The Hargreaves method shows negligible ET in barren western regions and 48.36 to 1,831.85 mm in other areas. The surface temperatures exhibiting the lowest temperature and highest ET correspond to vegetated areas, especially in northern parts where fields are well irrigated due to the availability of an abundance of surface water. Urban settlements, barren-rocky surfaces, and fallow farmlands exhibit greater LST but lower ET and lower NDVI (Figures 5 and 6).

5.2. Validation of SEBAL performance

The ET_o (crop reference evapotranspiration) value was computed using the FAO-PM formula and the Hargreaves method computed from the collected meteorological data for the IGNP region for the years 2019 and 2020. The mean ET_c values were calculated based on the growth stage of various crops from the data collected from the reports published by the

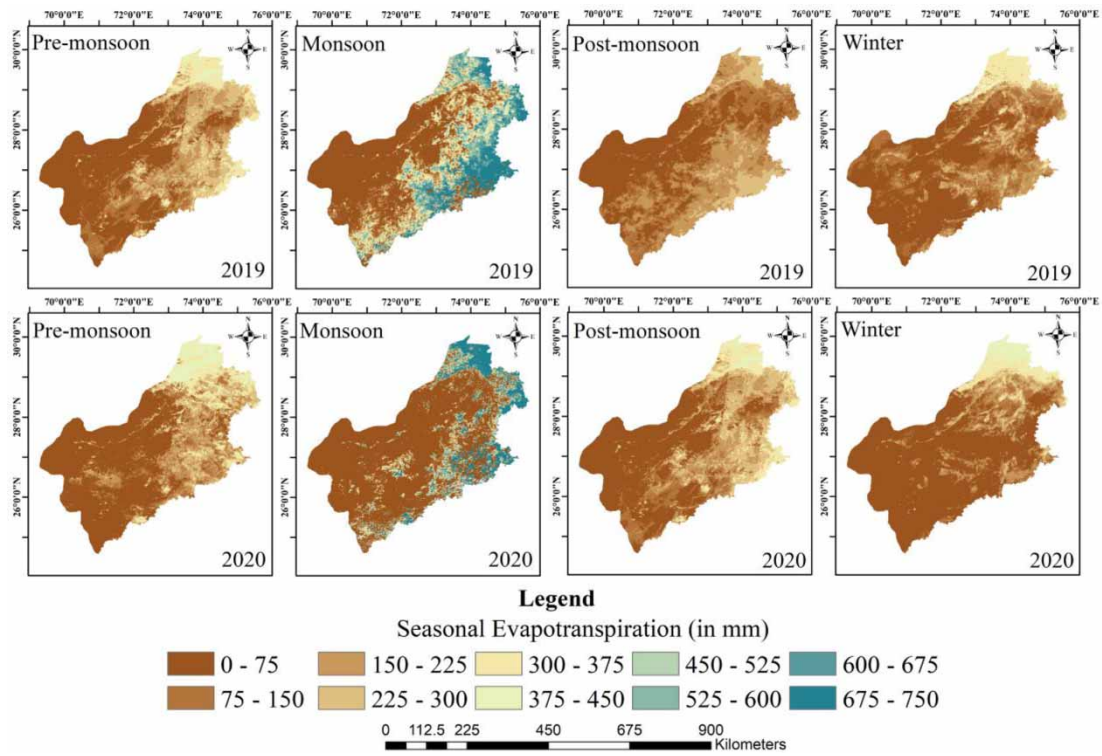


Figure 3 | Spatial distribution of seasonal evapotranspiration ET (in mm) for 2019 and 2020 using FAO Penman–Monteith.

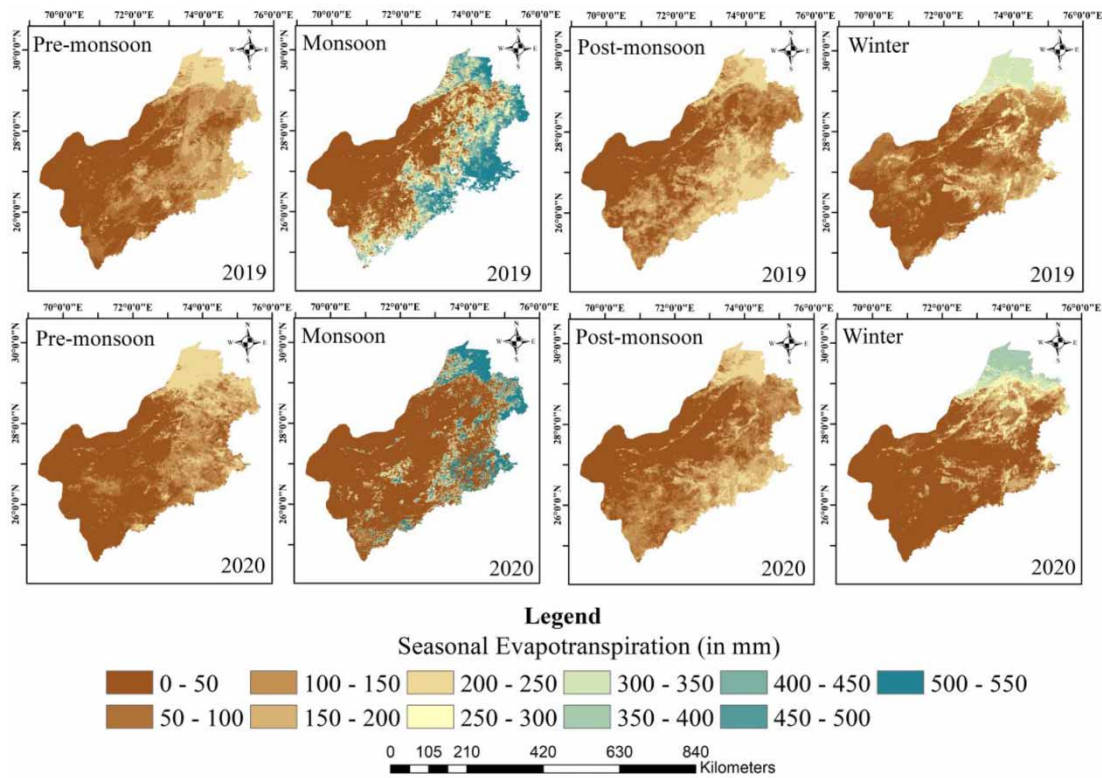


Figure 4 | Spatial distribution of seasonal evapotranspiration ET (in mm) for 2019 and 2020 using Hargreaves method.

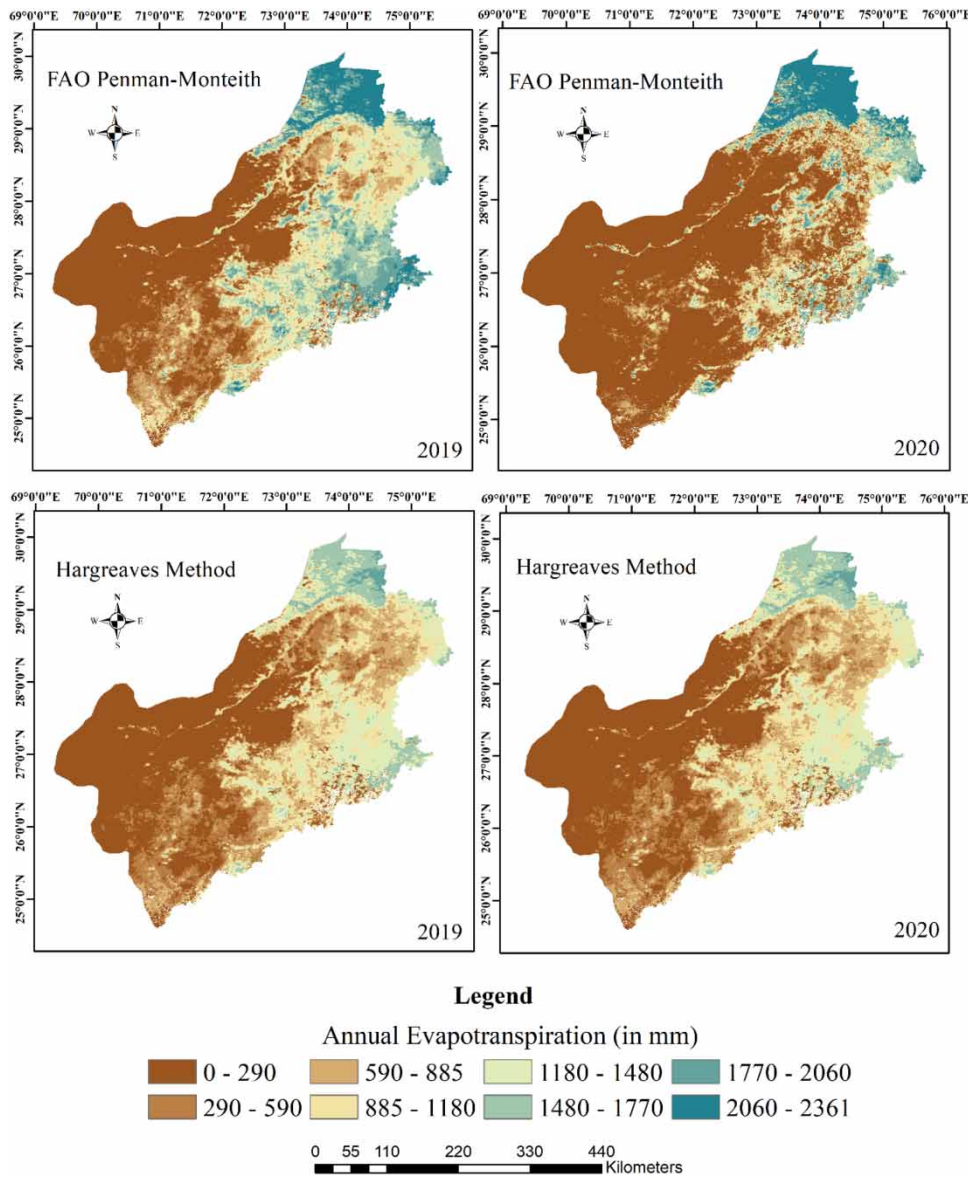


Figure 5 | Spatial distribution of annual evapotranspiration (in mm) using FAO Penman–Monteith and Hargreaves equations.

Department of Agriculture, which works under the Rajasthan state government for the years 2019 and 2020.

$$ET_c = ET_o \times K_c \tag{14}$$

where K_c is the crop factor, which varies based on the variety of crop, its growth phase, and the climate conditions, by means of three performance measure criteria – coefficient of determination, root-mean-squared error, and MBE – the daily ET generated with the SEBAL algorithm was examined to the values obtained from the preceding equation. Due to a lack of data concerning the spatial distribution of crops in the IGNP, validation of the SEBAL method at seasonal and regional scales was not possible in this work. The coefficient of determination R^2 is calculated using Equation (16). R^2 indicates the relative fit between ET_{SEBAL} and ET_{FAO} values.

$$R^2 = 1 - \frac{\sum_{i=1}^n (ET_{FAO} - ET_{SEBAL})^2}{\sum_{i=1}^n (ET_{FAO})^2} \tag{15}$$

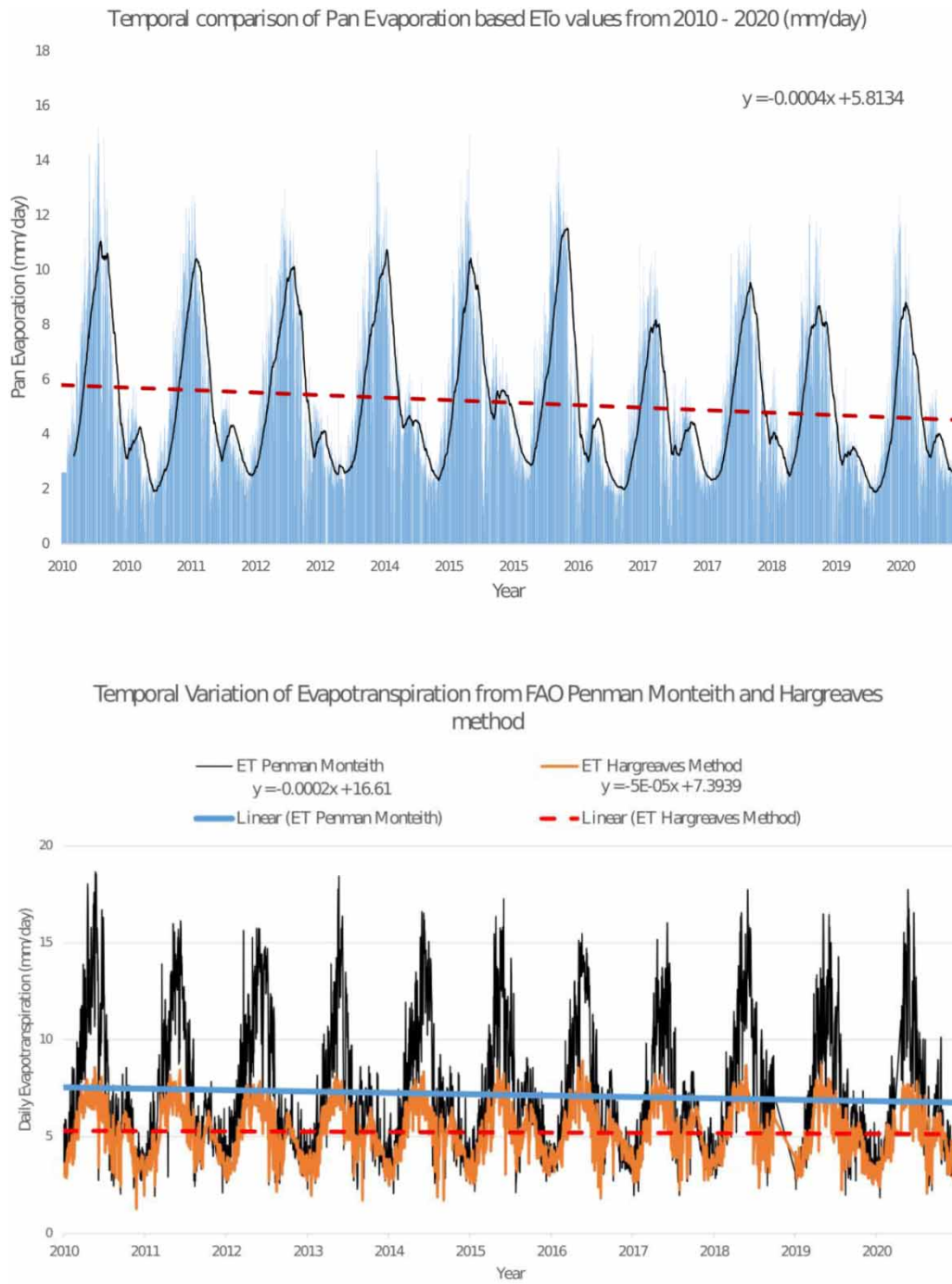


Figure 6 | Temporal variation of pan evaporation, FAO-PM, and Hargreaves equations based ET_o values from 2010 to 2020 (in mm/day).

The root-mean-square error (RMSE) is defined as ‘the square root of the residuals’ variance’. It indicates the algorithm’s actual fit with the data and the proximity of ET_{SEBAL} values to the ET_{FAO} values.

$$RMSE = \sqrt{\frac{\sum_{i=1}^n (ET_{FAO} - ET_{SEBAL})^2}{n}} \quad (16)$$

The MBE, a statistical criterion, is computed as

$$MBE = \frac{1}{N} \sum_{i=1}^N (ET_{FAO} - ET_{SEBAL}) \quad (17)$$

As demonstrated in Figure 7, the determination coefficient across SEBAL-estimated ET and estimates by the FAO-PM and Hargreaves techniques has an acceptable value of 0.84 for the Hargreaves method but shows a slight decrease of 0.60 for the FAO-PM method. Moreover, the RMSE value for the FAO-PM was computed as 3.99 mm day^{-1} and 0.05 mm day^{-1} for the Hargreaves method. Thus, these outcomes demonstrate the efficacy of the SEBAL model in calculating ET for the Western Rajasthan IGNP command region. It can be observed that bias was higher for the pre-monsoon season. This is due to the fact that the winter crops have been harvested, and most of the fields are fallow.

6. DISCUSSION

Evapotranspiration plays a major role in optimizing the irrigation management system and water balance. Sufficient information is scarce on the spatial distribution of ET. As per our knowledge, there is a huge lack of observed data on actual ET for the broad Western Rajasthan region, which is publicly available. Low ET is witnessed in the fallow lands during the pre-monsoon season as all the crops are harvested, whereas the monsoon and winter seasons demonstrate high values of ET as these are the crop-growing seasons in the region. In every season, water bodies exhibit extremely high ET. After the crop harvest, low ET is seen in fallow farmlands. The measured data by the meteorological station is scarce, and the estimation is valid just for the installed location. On the other hand, the SEBAL-based ET outputs are successful in covering a large spatial extent with satisfactory accuracy. As per our knowledge, there is a significant lack of publically available observed data on actual ET for the broad Western Rajasthan region. Low ET is witnessed in the fallow lands during the pre-monsoon season as all the crops are harvested, whereas the monsoon and winter seasons demonstrate high values of ET as these are the crop-growing seasons in the region. In every season, water bodies exhibit extremely high ET. After the crop harvest, low ET is seen in fallow farmlands. The measured data by the meteorological station is scarce, and the estimation is valid just for the installed location. On the other hand, the SEBAL-based ET outputs are successful in covering a large spatial extent with satisfactory accuracy.

In comparison to places with low or medium fractional vegetation cover, vegetated agricultural areas have a higher fractional vegetation cover, which leads to higher transpiration in the northern regions. Over agricultural regions, soil moisture also contributes to higher ET, whereas rocky surface areas and desert regions are mostly barren, exhibiting high surface temperatures and high sensible heat movement, which results in small ET. The SEBAL-generated ET and the Hargreaves technique of daily ET estimation have not been shown to differ significantly.

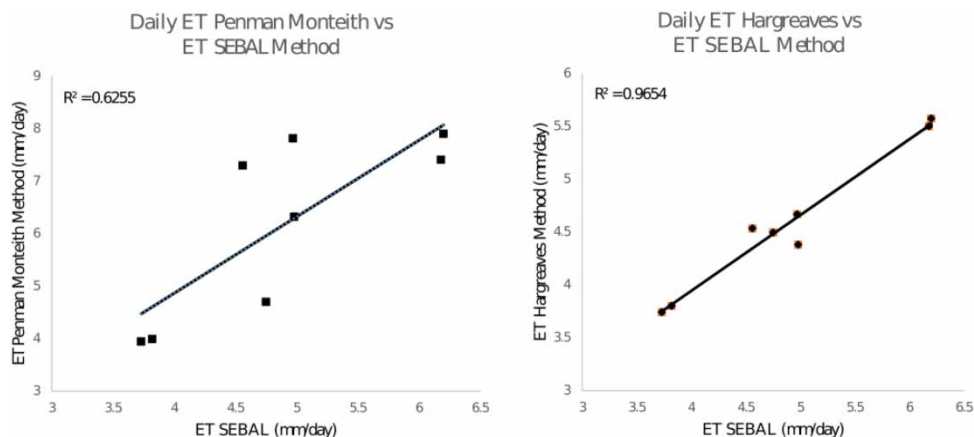


Figure 7 | Daily ET comparison between ET estimated FAO Penman–Monteith method (left) and ET from Hargreaves method (right) vs. ET estimated from SEBAL model.

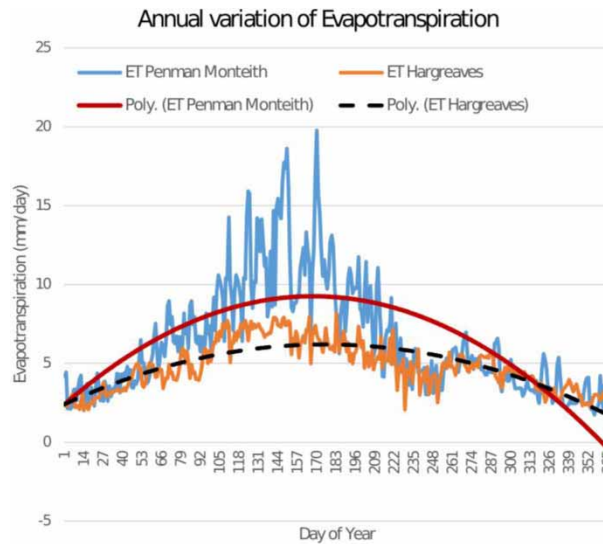


Figure 8 | Annual variation of evapotranspiration (in mm/day).

Figure 8 demonstrates the variation in ET rates (mm/day) for the entire year (2020). From January to mid-June, the second-degree polynomial trend shows that there is a progressive increase in daily ET values, followed by a fall from July to December. The highest ET is observed during the pre-monsoon season, followed by the monsoon season. Figure 6 shows the temporal variation of pan evaporation, FAO-PM, and Hargreaves method based ET_o values from 2010 to 2020 (in mm/day). The slope equation shows a downward trend in evapotranspiration rates from the region. The primary reasons for a downward trend in the pan evaporation data are the changing climatic conditions in the region, such as changes due to global climate and changes in the region over the last few decades (Saxena *et al.* 2023), which are witnessing significant effects on ET_o , which is controlled by developments in the aerodynamic elements. The most influential meteorological variables on ET_o trends in the region were determined to be variations in wind speed and relative humidity. Similar observations have been made in various other studies (Goroshi *et al.* 2017).

7. CONCLUSION

The model developed is a semi-automated, flexible, user-friendly ET retrieval system with high spatial resolution. The main features of this model include spatial coverage over a large extent, such as the IGNP region, estimation of various vegetation indices, emissivity, LST, and actual ET, specifically in arid and semi-arid regions experiencing low wind speeds with readily available Landsat-8 and MODIS images, which would have required huge computational resources if applied using the conventional methods. The advantage of employing such a model is to acquire the desired ET data with its high resolution and spatiotemporal variations, particularly in regions having scarce weather and soil moisture data. The valuable facts and data will assist in optimizing water management at any scale for the IGNP command region. The results can be used for irrigation management by identifying the areas and seasons with high ET rates, indicating higher water demand. Temporal patterns of ET can be used for drought monitoring. A sudden decrease in ET might indicate water stress in vegetation. Monitoring these patterns over time can help anticipate and manage drought conditions effectively. Changes in spatiotemporal ET patterns can be indicative of climate change impacts. Monitoring these changes over the years can contribute to climate change impact assessments, helping communities adapt to new conditions for sustainable development. The present study assesses the remodeling of the deserted region into agriculturally and socioeconomically productive land, which fits well with the ‘Sustainable Development Goals’ (SDG) and the targets anticipated by the UN for the year 2030. The SEBAL-based model was calibrated and authenticated for the different seasons with an accuracy of more than 96% compared to the suggested Hargreaves method. The overall trend analyzed from the available weather data (pan evaporation) shows a downward trend in the rate of evapotranspiration (2010–2020). In summary, the spatial and temporal patterns of evapotranspiration are valuable for making informed decisions regarding water management, land use planning, and adapting to changing environmental conditions. These insights contribute to more sustainable and efficient water use in a region. The future scope of this

study can be used to generate new climate parameters as a result of altering other SEBAL characteristics. Alternative climatic and land use change scenarios, as well as seasonal fluctuation in land use changes, might be taken into account as potential future scenarios. Agricultural lands differ in crop cover, which results in varying rates of actual ET values and can serve as a future research topic.

DATA AVAILABILITY STATEMENT

Data cannot be made publicly available; readers should contact the corresponding author for details.

CONFLICT OF INTEREST

The authors declare there is no conflict.

REFERENCES

- Agricultural Statistics 2020 *Agricultural_Statistics_2019-20*. Department of Planning, Government of Rajasthan, India.
- Allen, R. G., Pereira, L. S., Raes, D. & Smith, M. 1998 *FAO Irrigation and Drainage Paper*, Vol. 56. Food and Agriculture Organization of the United Nations, Rome, p. 327.
- Allen, R. G., Morse, A., Tasumi, M., Trezza, R., Bastiaanssen, W., Wright, J. L. & Kramer, W. 2005a Evapotranspiration from a satellite-based surface energy balance for the snake plain aquifer in Idaho. *California Water Plan Update* **4**, 16.
- Allen, R. G., Tasumi, M. & Morse, A. 2005b Satellite-based evapotranspiration by METRIC and Landsat for western states water management, p. 20.
- Amarasinghe, U. A., Shah, T., Turrall, H. & Anand. B. K. 2007 *India's Water Future to 2025-2050: Business-as-Usual Scenario and Deviations*. International Water Management Institute, Colombo, Sri Lanka.
- Aryalekshmi, B. N., Biradar, R. C., Chandrasekar, K. & Mohammed Ahamed, J. 2021 [Analysis of various surface energy balance models for evapotranspiration estimation using satellite data](#). *The Egyptian Journal of Remote Sensing and Space Science* **24** (3, Part 2), 1119–1126.
- Babatunde, E. B. 2012 *Solar Radiation*. Intech, Rijeka, Croatia.
- Bastiaanssen, W. G. M. 2000 SEBAL-based sensible and latent heat fluxes in the irrigated Gediz Basin, Turkey. *Journal of Hydrology* **229** (1–2), 87–100.
- Bastiaanssen, W. G. M., Menenti, M., Feddes, R. A. & Holtslag, A. A. M. 1998 [A remote sensing surface energy balance algorithm for land \(SEBAL\). 1. Formulation](#). *Journal of Hydrology* **212–213**, 198–212.
- Beaumont, P., Blake, G. & Wagstaff, J. M. 2016 *The Middle East*, 0 edn. Routledge, Oxford.
- Bhattarai, N., Quackenbush, L. J., Dougherty, M. & Marzen, L. J. 2015 [A simple Landsat–MODIS fusion approach for monitoring seasonal evapotranspiration at 30m spatial resolution](#). *International Journal of Remote Sensing* **36** (1), 115–143.
- Bowen, I. S. 1926 [The ratio of heat losses by conduction and by evaporation from any water surface](#). *Physical Review* **27** (6), 779–787.
- Crago, R. D. 1996 [Conservation and variability of the evaporative fraction during the daytime](#). *Journal of Hydrology* **180** (1), 173–194.
- Crop Wise Sowing Area Report, G. 2020 *Crop Wise Sowing Area*. *Agricultural Statistics 2020–21*. Directorate of Economics & Statistics, Rajasthan, Jaipur, India.
- Dhungal, R., Allen, R. G. & Trezza, R. 2016 [Improving iterative surface energy balance convergence for remote sensing based flux calculation](#). *Journal of Applied Remote Sensing* **10** (2), 026033.
- Droogers, P. & Allen, R. G. no date [Estimating reference evapotranspiration under inaccurate data conditions](#). *Irrigation and Drainage Systems* **16**, 33–45.
- Elkatoury, A., Alazba, A. A. & Mossad, A. 2020 [Estimating evapotranspiration using coupled remote sensing and three SEB models in an arid region](#). *Environmental Processes* **7** (1), 109–133.
- Gao, F., Feng, G., Ouyang, Y., Wang, H., Fisher, D., Adeli, A. & Jenkins, J. 2017 [Evaluation of reference evapotranspiration methods in arid, semiarid, and humid regions](#). *JAWRA Journal of the American Water Resources Association* **53** (4), 791–808.
- Gorelick, N., Hancher, M., Dixon, M., Ilyushchenko, S., Thau, D. & Moore, R. 2017 [Google Earth Engine: Planetary-scale geospatial analysis for everyone](#). *Remote Sensing of Environment* **202**, 18–27.
- Goroshi, S., Pradhan, R., Singh, R. P., Singh, K. K. & Parihar, J. S. 2017 [Trend analysis of evapotranspiration over India: Observed from long-term satellite measurements](#). *Journal of Earth System Science* **126** (8), 113.
- Jangid, M., Sharma, L., Burark, S., Hk, J., Meena, G. & Mundra, S. 2018 [Comparing performance of various crops in Rajasthan state based on market price, economic prices and natural resource valuation](#). *Economic Affairs* **63**, 709–716.
- Jiang, L., Zhang, B., Han, S., Chen, H. & Wei, Z. 2021 [Upscaling evapotranspiration from the instantaneous to the daily time scale: Assessing six methods including an optimized coefficient based on worldwide eddy covariance flux network](#). *Journal of Hydrology* **596**, 126135.
- Jiménez-Muñoz, J. C., Sobrino, J. A., Skoković, D., Mattar, C. & Cristóbal, J. 2014 [Land surface temperature retrieval methods from Landsat-8 thermal infrared sensor data](#). *IEEE Geoscience and Remote Sensing Letters* **11** (10), 1840–1843.
- Johnson, L. F. & Trout, T. J. 2012 [Satellite NDVI assisted monitoring of vegetable crop evapotranspiration in California's San Joaquin Valley](#). *Remote Sensing* **4** (2), 439–455.

- Kalluri, S. N. V., Townshend, J. R. G. & Doraiswamy, P. 1998 A simple single layer model to estimate transpiration from vegetation using multi-spectral and meteorological data. *International Journal of Remote Sensing* **19** (6), 1037–1053.
- Kumar, D. & Shekhar, S. 2015 Statistical analysis of land surface temperature–vegetation indexes relationship through thermal remote sensing. *Ecotoxicology and Environmental Safety* **121**, 39–44.
- Kundu, S., Mondal, A., Khare, D., Hain, C. & Lakshmi, V. 2018 Projecting climate and land use change impacts on actual evapotranspiration for the Narmada River Basin in central India in the future. *Remote Sensing* **10** (4), 578.
- Li, Z.-L., Tang, R., Wan, Z., Bi, Y., Zhou, C., Tang, B., Yan, G. & Zhang, X. 2009 A review of current methodologies for regional evapotranspiration estimation from remotely sensed data. *Sensors* **9** (5), 3801–3853.
- Liu, Z. 2021 The accuracy of temporal upscaling of instantaneous evapotranspiration to daily values with seven upscaling methods. *Hydrology and Earth System Sciences* **25** (8), 4417–4433.
- Lv, M., Xu, Z. & Lv, M. 2021 Evaluating hydrological processes of the atmosphere–vegetation interaction model and MERRA-2 at global scale. *Atmosphere* **12** (1), 16.
- Moharana, P., Santra, P., Singh, D., Kumar, S., Goyal, R., Machiwal, D. & Yadav, O. P. 2016 ICAR-Central Arid Zone Research Institute, Jodhpur: Erosion processes and desertification in the Thar Desert of India. *Proceedings of the Indian National Science Academy* **82**, 1117–1140.
- Null, N. 1996 *Hydrology Handbook*. American Society of Civil Engineers, New York.
- Pereira, L. S., Allen, R. G., Smith, M. & Raes, D. 2015 Crop evapotranspiration estimation with FAO56: Past and future. *Agricultural Water Management* **147**, 4–20.
- Physical Progress 2020 *Rajasthan Water Sector Restructuring Project (RWSRPD)*. Government of Rajasthan, Rajasthan.
- Rahimi, S., Gholami Sefidkouhi, M. A., Raeini-Sarjaz, M. & Valipour, M. 2015 Estimation of actual evapotranspiration by using MODIS images (a case study: Tajan catchment). *Archives of Agronomy and Soil Science* **61** (5), 695–709.
- Rao, A. S. & Poonia, S. 2011 Climate change impact on crop water requirements in arid Rajasthan. *Journal of Agrometeorology* **13** (1), 17–24.
- Saxena, D., Choudhary, M. & Sharma, G. 2023 Land use and land cover change impact on characteristics of surface evapotranspiration in semi-arid environment of Western Rajasthan, India. *Water Practice and Technology* **19** (1), 154–169.
- Shahrokhnia, M. H. & Sepaskhah, A. R. 2013 Single and dual crop coefficients and crop evapotranspiration for wheat and maize in a semi-arid region. *Theoretical and Applied Climatology* **114** (3–4), 495–510.
- Shamloo, N., Taghi Sattari, M., Apaydin, H., Valizadeh Kamran, K. & Prasad, R. 2021 Evapotranspiration estimation using SEBAL algorithm integrated with remote sensing and experimental methods. *International Journal of Digital Earth* **14** (11), 1638–1658.
- Shapland, T. M., Snyder, R. L., Paw U, K. T. & McElrone, A. J. 2014 Thermocouple frequency response compensation leads to convergence of the surface renewal alpha calibration. *Agricultural and Forest Meteorology* **189–190**, 36–47.
- Silva, B. B. d., Montenegro, S. M. G. L., Silva, V. d. P. R. d., Rocha, H. R. d., Galvncio, J. D. & Oliveira, L. M. M. d. 2015 Determination of instantaneous and daily net radiation from TM – Landsat 5 data in a subtropical watershed. *Journal of Atmospheric and Solar-Terrestrial Physics* **135**, 42–49.
- Silva, B. B. d., Braga, A. C., Braga, C. C., Oliveira, L. M. M. d., Montenegro, S. M. G. L. & Barbosa Junior, B. 2016 Procedures for calculation of the albedo with OLI-Landsat 8 images: Application to the Brazilian semi-arid. *Revista Brasileira de Engenharia Agrcola E Ambiental* **20**, 3–8.
- Tran, D. X., Pla, F., Latorre-Carmona, P., Myint, S. W., Caetano, M. & Kieu, H. V. 2017 Characterizing the relationship between land use land cover change and land surface temperature. *ISPRS Journal of Photogrammetry and Remote Sensing* **124**, 119–132.
- Wanniarachchi, S. & Sarukkalgige, R. 2022 A review on evapotranspiration estimation in agricultural water management: Past, present, and future. *Hydrology* **9** (7), 123.
- Wilson, K., Goldstein, A., Falge, E., Aubinet, M., Baldocchi, D., Berbigier, P., Bernhofer, C., Ceulemans, R., Dolman, H., Field, C., Grelle, A., Ibrom, A., Law, B. E., Kowalski, A., Meyers, T., Moncrieff, J., Monson, R., Oechel, W., Tenhunen, J., Valentini, R. & Verma, S. 2002 Energy balance closure at FLUXNET sites. *Agricultural and Forest Meteorology* **113** (1), 223–243.
- Wu, C.-D., Cheng, C.-C., Lo, H.-C. & Chen, Y.-K. 2010 Application of SEBAL and Markov models for future stream flow simulation through remote sensing. *Water Resources Management* **24**, 3773–3797.
- Zhang, L., Traore, S., Cui, Y., Luo, Y., Zhu, G., Liu, B., Fipps, G., Karthikeyan, R. & Singh, V. 2019 Assessment of spatiotemporal variability of reference evapotranspiration and controlling climate factors over decades in China using geospatial techniques. *Agricultural Water Management* **213**, 499–511.

First received 2 September 2023; accepted in revised form 13 February 2024. Available online 26 February 2024